PCCP

ROYAL SOCIETY OF CHEMISTRY

PAPER

View Article Online
View Journal | View Issue

Cite this: *Phys. Chem. Chem. Phys.*, 2026, **28**, 8478

Noncovalent chemical chameleons in action: positive cooperativity of trifurcated halogen bonds in 2I···I···Nu assemblies

Nadezhda A. Bokach, [a] Vadim Yu. Kukushkin, [ab] Rosa M. Gomila [c] and Antonio Frontera *[c]

While multicenter halogen bonds typically exhibit negative cooperativity in donor-only systems, crystallographic surveys reveal robust hetero-atomic assemblies featuring the 2I···I···Nu motif (Nu = N, O, S, and C). Here we present a comprehensive theoretical investigation of this bonding pattern to evaluate its intrinsic electronic synergy. We initially performed a systematic density functional theory (DFT) analysis on fully optimized model systems involving diatomic iodine (I_2) and the iodine trimer ($(I_2)_3$) acting as σ-hole donors, interacting with a series of small, linear Lewis bases (HF, CO, HCN, OCN^-, SCN^-, and $SeCN^-$). Our calculations on these optimized models demonstrate that the $(I_2)_3$ trimer functions as a significantly stronger σ-hole donor than the isolated I_2 molecule, confirming pronounced positive cooperativity. To validate these findings in the solid state, we extended the analysis to two representative crystal structures: a homotrimeric 2,4,5-triiodoimidazole assembly (UNOMIV) and a cocrystal of 1,3,5-triiodo-2,4,6-trifluorobenzene with 1,4-dithiane (ZAQZOK). Energy decomposition analysis and quantum theory of atoms in molecules results for these crystallographic systems mirror the trends observed in the model complexes. Specifically, the formation of flanking I···I contacts amplifies the σ-hole depth of the central iodine atom, increasing it from 21.9 to 24.8 kcal mol^{-1} in UNOMIV and from 30.1 to 33.9 kcal mol^{-1} in ZAQZOK. Natural bond orbital analysis confirms that charge transfer from the central iodine's lone pairs to the antibonding σ* orbitals of the flanking molecules drives this synergistic behavior. These findings validate the chemical chameleon property as a foundation for crystal engineering, establishing the 2I···I···Nu motif as a robust supramolecular synthon.

Received 22nd December 2025,
Accepted 3rd March 2026

DOI: 10.1039/d5cp04988a

rsc.li/pccp

Introduction

When covalently bound to electron-withdrawing groups, halogen atoms develop a pronounced asymmetry in their electron distribution that fundamentally alters their interaction capabilities.[1,2] This asymmetry generates two distinct electrostatic regions on the halogen surface: a region of positive potential (the σ-hole) extending along the covalent bond axis and a belt of negative potential encircling the atom perpendicular to this axis.[3–5] The depth of the σ-hole grows progressively from F to I, correlating with increasing atomic polarizability. Consequently, iodine exhibits the strongest directional binding capacity among the halogens.

This electrophilic–nucleophilic dualism allows a single halogen atom to engage in multiple binding modes depending on its molecular environment.[3] The positive σ-hole region attracts electron-rich partners such as lone pairs or π-systems, while the negative equatorial belt can interact with electron-poor sites. A consequence of this versatility appears in systems where one halogen atom acts as both a donor and an acceptor simultaneously, behavior that has led to the description of activated halogens as chemical chameleons.[2,6,7] Such arrangements represent an important design element for constructing complex supramolecular architectures.

In our recent review,[2] we classified multicenter halogen-bonded assemblies based on the role of the central halogen atom. In donor-only systems, a single σ-hole interacts with multiple nucleophiles, typically exhibiting negative cooperativity due to competition for electron density.[8] This negative cooperativity limits the utility of donor-only systems for supramolecular design.

A well-known manifestation of simultaneous donor–acceptor behavior occurs in polyhalide assemblies. Solid iodine and

[a] *Institute of Chemistry, Saint Petersburg State University, Universitetskaya Nab. 7/9, 199034 Saint Petersburg, Russian Federation*
[b] *Institute of Chemistry and Pharmaceutical Technologies, Altai State University, 656049 Barnaul, Russian Federation*
[c] *Departament de Química, Universitat de les Illes Balears, Crta de Valldemossa km 7.5, 07122 Palma de Mallorca (Baleares), Spain. E-mail: toni.frontera@uib.es*

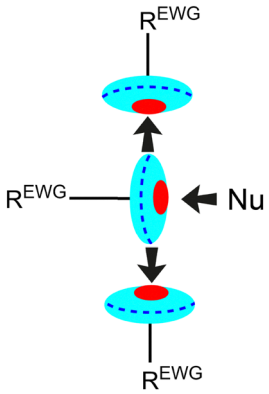

Fig. 1 Schematic representation of the 2I···I···Nu (Nu = N, O, S, or C) trifurcated four-center nodes.

polyiodide anions (I_3^-, I_5^-, *etc.*) form extended networks through complementary σ-hole···electron belt contacts, where each I atom participates as both a donor and an acceptor.[9] These systems provided early evidence for the chemical chameleon concept but are inherently limited to purely halogen-based architectures.

A fundamentally different situation arises in mixed donor–acceptor systems incorporating heteroatomic nucleophiles. In our review,[2] we systematically analyzed the Cambridge Structural Database (CSD) and identified the 2I···I···Nu motif (where Nu = N, O, S, or C nucleophilic atom) as a particularly robust example of such architecture. In these assemblies (Fig. 1), a central I atom donates through its σ-hole to a nucleophilic partner while simultaneously receiving electron density from two flanking I atoms *via* its equatorial belt. This trifurcated bonding pattern creates a four-atom node that serves as a fundamental building block for extended supramolecular architectures.

Although crystallographic data confirm that the 2I···I···Nu assemblies are geometrically viable, they cannot address a key question: do the individual interactions within this unit reinforce or weaken each other? Given the negative cooperativity observed in donor-only bifurcated systems, it remained unknown whether the same limitation applies to mixed donor–acceptor nodes.

Here we address this question by first performing a systematic quantum chemical analysis on fully optimized model systems. To evaluate the intrinsic electronic properties of the 2I···I···Nu motif free from steric hindrance and crystal packing forces, we computed halogen-bonded complexes involving diatomic iodine (I_2) and the iodine trimer ($(I_2)_3$) acting as σ-hole donors. These were paired with a series of small, linear Lewis bases (HF, CO, HCN, OCN^-, SCN^-, and $SeCN^-$) acting as electron donors (σ-hole acceptors). Comparisons between the isolated I_2 and the $(I_2)_3$ trimer allowed us to determine how the formation of the iodine cluster modifies the σ-hole capability of the central iodine atom in the absence of bulky substituents.

Subsequently, to confirm that this synergy persists in realistic supramolecular environments, we analyzed representative

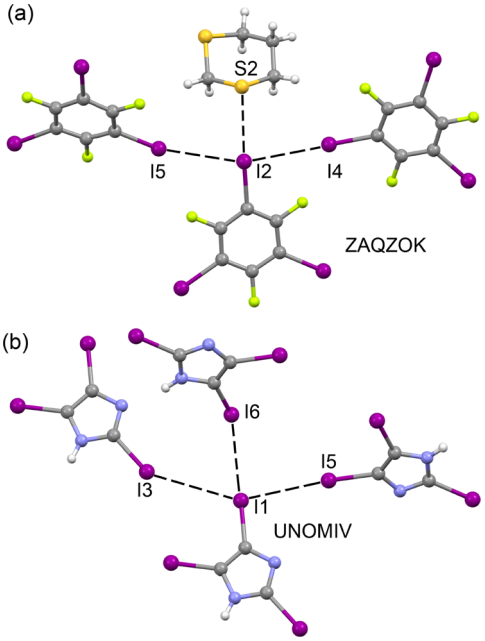

Fig. 2 Fragments of the crystal structures of ZAQZOK (a) and UNOMIV (b) showing the trifurcated four-center node.

crystal structures identified in our structural analysis.[2] We selected two systems (Fig. 2), CSD refcode UNOMIV[10] (a homotrimeric iodoimidazole assembly) and CSD refcode ZAQZOK[11] (a cocrystal of triiodofluorobenzene with dithiane), and applied density functional theory (DFT) combined with natural bond orbital (NBO) analysis, atoms-in-molecules topology (QTAIM), and energy decomposition (EDA) methods.

Our results across both the optimized models and the crystallographic systems reveal that the flanking I···I contacts amplify the σ-hole depth on the central iodine, leading to a strengthened primary interaction with the nucleophile. This positive cooperativity distinguishes the 2I···I···Nu motif from conventional bifurcated halogen bonds and validates the chemical chameleon concept as a practical foundation for crystal engineering.

Methods

The solid state calculations were performed using the TURBOMOLE 7.7 software package.[12] The PBE0[13] hybrid functional was employed in conjunction with the def2-TZVP basis set for all atoms[14] including relativistic effects in the ECPs for iodine. The D4 dispersion correction[15] was applied to account for long-range interactions. The I_2 and $(I_2)_3$ compounds and complexes were optimized while for the calculations of UNOMIV and ZAQZOK we used the X-ray crystallographic data to analyze the synergistic effects as they exist in the solid state. For the $(I_2)_3$ complexes, $(I_2)_3$ was considered as a monomeric unit for the calculations of the interaction energies and its geometry was kept frozen in the complexes to avoid the migration of the flanked I_2 units to the approaching nucleophile, which only occurs for anionic donors. Energy decomposition analysis

(EDA) was performed using the Kitaura–Morokuma method.[16] The densest multiple grid available in Turbomole was used (m5) with very tight settings, for SCF convergence. Molecular electrostatic potential (MEP) surfaces were generated at the same level of theory, using an isovalue of 0.001 a.u. natural bond orbital (NBO)[17] analysis was conducted using the NBO7 program.[18] Quantum theory of atoms in molecules (QTAIM)[19] and electron localization function (ELF) analyses were performed with the Multiwfn program.[20]

The calculation of the interaction energies and QTAIM parameters was also performed using the CCSD(T)/def2-TZVP level of theory using the ORCA 6.0 program[21] and PBE0-D4/def2-TZVP geometries.

Results and discussion

Preliminary DFT analysis

To provide a fundamental understanding of the cooperative effects in 2I···I···Nu assemblies without the influence of crystal packing or steric effects from bulky substituents, we first analyzed fully optimized model systems based on diatomic iodine. We compared the isolated iodine molecule (I_2) with a trimeric assembly ($(I_2)_3$) where a central I_2 unit is flanked by two others, mimicking the chameleon motif. The MEP surfaces (Fig. 3) provide clear evidence of the electronic redistribution that drives cooperativity. In the isolated I_2 monomer, the maximum potential at the σ-hole is 32.6 kcal mol^{-1}. Upon formation of the trimeric $(I_2)_3$ assembly, this value increases significantly to 40.8 kcal mol^{-1}. This enhancement is rationalized by the charge transfer from the central iodine's lone pairs to the antibonding σ* orbitals of the flanking iodine molecules. This electron donation depletes electron density from the central iodine, thereby intensifying its σ-hole. Consequently, the flanking iodine atoms, acting as acceptors, exhibit an increase in electron density, reflected by a deepening of their equatorial belt potential from −4.1 kcal mol^{-1} in the monomer to −6.2 kcal mol^{-1} in the trimer.

Following the electrostatic analysis, we evaluated the impact of this σ-hole activation on the binding ability of the iodine units. We modeled the interaction of both the isolated I_2 and the $(I_2)_3$ trimer with a series of linear Lewis bases varying in electronic nature: neutral species (HF, CO, and HCN) and anionic pseudohalides (OCN^-, SCN^-, and $SeCN^-$). This resulted in two series of complexes: the monomeric adducts **1–7** and the trimeric analogues **8–14** (Scheme 1).

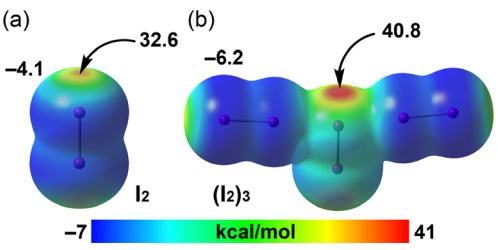

Fig. 3 MEP surfaces (0.001 a.u. isovalue) for the optimized (a) isolated iodine molecule (I_2) and (b) iodine trimer ($(I_2)_3$). The energies at the designated points (σ-hole maxima and belt minima) are given in kcal mol^{-1}. The color scale ranges from −7 (blue) to 41 (red) kcal mol^{-1}.

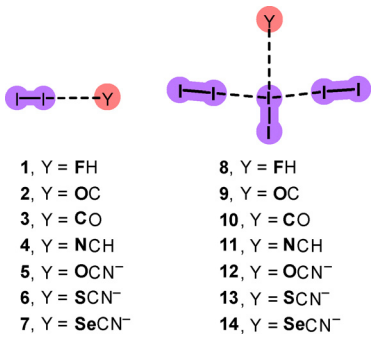

Scheme 1 Schematic representation of the computed halogen-bonded complexes.

The geometric and energetic data for these complexes are summarized in Table 1. To ensure a direct comparison, the interaction energies (E_{int}) for the trimeric complexes (**8–14**) were computed by treating the $(I_2)_3$ moiety as a single rigid fragment. While the $(I_2)_3$ moiety was kept frozen during the systematic energy comparison to ensure consistency across the neutral and anionic series, we investigated the structural stability of these motifs through full geometry optimizations. For neutral systems, the 2I···I···Nu trifurcated assembly remains a stable local minimum on the potential energy surface. For the anionic complexes **12–14**, the gas-phase optimization leads to a structural migration where the flanking I_2 units shift toward the central nucleophile. As illustrated in Fig. 4 for complex **12**, the resulting geometry features a central Y-atom involved in three concurrent Y···I_2 contacts, and QTAIM analysis confirms the presence of trifurcated halogen bonds.

The results in Table 1 consistently demonstrate positive cooperativity, aligning perfectly with the MEP predictions. In all cases, the interaction energy is significantly strengthened upon moving from the monomeric to the trimeric donor. For instance, the weak interaction with HF increases from

Table 1 Energetic and geometric features of complexes **1–14** at the PBE0-D4/def2-TZVP and CCSD(T)/def2-TZVP//PBE0-D4/def2-TZVP levels of theory. Interaction and second order perturbation energies (E_{int} and $E^{(2)}$ LP(Y) → σ*(I–I), respectively) are given in kcal mol^{-1}. I···Y distance (d) in Å. The density at the bond critical point connecting Y to I (ρ) in a.u.

cmpd	Y	d	E_{int} DFT	E_{int} CCSD(T)	ρ DFT	ρ CCSD(T)	$E^{(2)}$
1	HF	3.146	−2.3	−2.1	0.0075	0.0070	1.2
2	OC	3.396	−1.2	−1.2	0.0054	0.0050	0.8
3	CO	3.094	−2.8	−2.1	0.0162	0.0153	7.4
4	HCN	2.954	−4.4	−3.9	0.0179	0.0165	6.3
5	OCN^-	2.389	−20.1	−18.1	0.0472	0.0426	25.0
6	SCN^-	2.989	−10.2	−9.4	0.0232	0.0209	11.8
7	$SeCN^-$	3.169	−8.3	−8.0	0.0186	0.0162	8.0
8	HF	3.024	−3.6	−3.3	0.0100	0.0093	1.9
9	OC	3.309	−2.0	−2.0	0.0066	0.0061	1.1
10	CO	3.055	−4.1	−3.2	0.0178	0.0168	8.9
11	HCN	2.862	−6.9	−6.0	0.0220	0.0203	9.0
12	OCN^-	2.343	−29.0	−25.7	0.0531	0.0479	29.2
13	SCN^-	2.884	−17.3	−15.3	0.0302	0.0265	17.1
14	$SeCN^-$	3.035	−14.9	−13.5	0.0249	0.0218	12.9

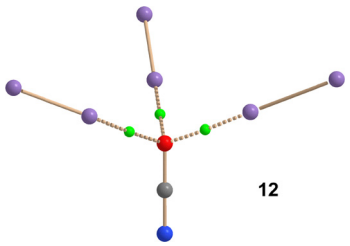

Fig. 4 Fully optimized complex **12** and its QTAIM analysis showing the trifurcated halogen bonds. BCPs are represented as green spheres and bond paths as dashed bonds.

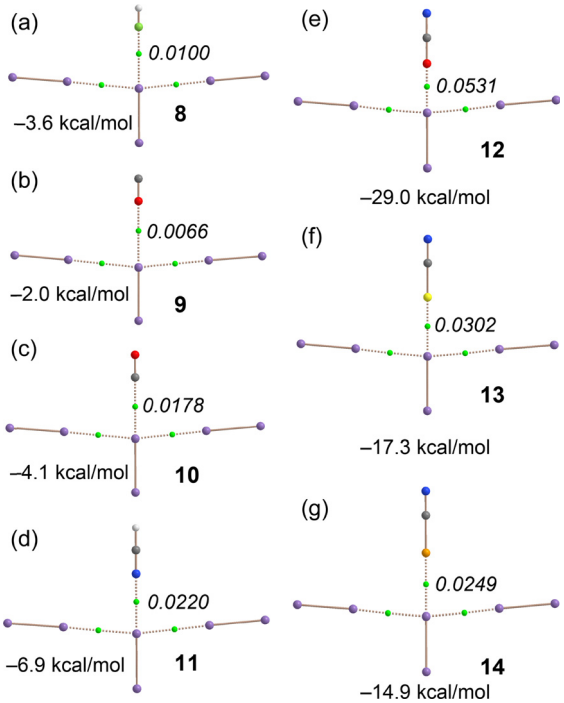

Fig. 5 QTAIM analysis (PBE0-D4/def2-TZVP) of compounds **8–14** (a–g, respectively), evidencing the halogen bonding with the flanking iodines and the halogen bond with the nucleophile. The density values are given in italics close to the BCPs for the I···Y halogen bonds in a.u.

–2.3 kcal mol^{-1} in complex **1** to –3.6 kcal mol^{-1} in complex **8**. This trend is even more pronounced for strong nucleophiles; the interaction with the cyanate anion (OCN^-) intensifies from –20.1 kcal mol^{-1} in the monomeric complex **5** to –29.0 kcal mol^{-1} in the trimeric assembly **12**. To validate the DFT interaction energies and the small reinforcement observed in several complexes, we employed the CCSD(T)/def2-TZVP//PBE0-D4/def2-TZVP level of theory. The results show that the energies are qualitatively similar between both methods, with a standard deviation of 0.94 kcal mol^{-1}. These findings align with previous benchmarking studies on halogen bonding.[22] More importantly, the differences between the dimers and tetramers (the cooperative reinforcement) are also very similar, showing a standard deviation of only 0.48 kcal mol^{-1}. For instance, in the complexes exhibiting the smallest reinforcement (**2** *vs.* **9**), the DFT and CCSD(T) methods provide identical values. This demonstrates that the reported energy differences are not artifacts of the DFT functional but represent genuine electronic effects.

This energetic reinforcement is accompanied by consistent structural tightening. The intermolecular distances (d) between the iodine σ-hole donor and the nucleophilic atom (Y) are uniformly shorter in the trimeric complexes compared to their monomeric counterparts. For example, the I···N distance in the HCN complexes shortens from 2.954 Å (**4**) to 2.862 Å (**11**), reflecting a stronger noncovalent bond.

Topological analysis using QTAIM further corroborates this strengthening (see Fig. 5). The electron density (ρ) at the bond critical point (BCP) connecting the iodine to the nucleophile (represented as a small green sphere in Fig. 5) is consistently higher in the $(I_2)_3$ complexes. For the $SeCN^-$ series, ρ increases from 0.0186 a.u. in complex **7** to 0.0249 a.u. in complex **14**, indicating a greater accumulation of electron density in the bonding region. Topological analysis using the CCSD(T) density further corroborates these findings, as the ρ values show similar increments in electron density at the bond critical points for the $(I_2)_3$ complexes compared to the dimers.

Finally, NBO analysis provides insight into the orbital origins of this cooperativity. The second-order perturbation energies ($E^{(2)}$) corresponding to the charge transfer from the lone pair of the Lewis base to the antibonding σ* orbital of the iodine donor (LP(Y) → σ*(I–I); LP is lone pair) are consistently larger for the trimeric systems. This enhancement confirms that the polarization induced by the flanking iodine molecules lowers the energy of the central σ*(I–I) orbital, thereby making it a better acceptor for the incoming nucleophile. As expected, the magnitude of these charge transfer energies is substantially larger for the anionic donors (*e.g.*, 29.2 kcal mol^{-1} for **12**) compared to the neutral ones (*e.g.*, 8.9 kcal mol^{-1} for **10**), but the cooperative enhancement remains a systematic feature across the entire series.

To further rationalize the trends observed in the monomeric and trimeric complexes, we performed a regression analysis connecting the energetic parameters with the topological and orbital descriptors derived from QTAIM and NBO calculations (Fig. 6). The first plot (Fig. 6a) reveals a strong linear correlation [r = 0.954 using DFT, r = 0.939 using CCSD(T)] between the electron density (ρ) at the bond critical point connecting the iodine donor to the nucleophile and the total interaction energy (E_{int}). This direct relationship indicates that the magnitude of electron accumulation at the intermolecular interface is a reliable indicator of bond strength.

Consequently, the increased ρ values observed in the trimeric complexes (**8–14**) compared to the monomers (**1–7**) serve as robust quantitative predictors of the positive cooperativity inherent to the 2I···I···Nu motif. The second plot (Fig. 6b) demonstrates an equally strong correlation [r = 0.961, slope ≈ 1.00 using DFT; r = 0.955 slope = 0.93 CCSD(T)] between the interaction energy and the NBO second-order perturbation energy ($E^{(2)}$) associated with the LP(Y) → σ*(I–I) charge transfer. This finding is particularly significant as it links the binding strength directly to orbital interactions. The linearity

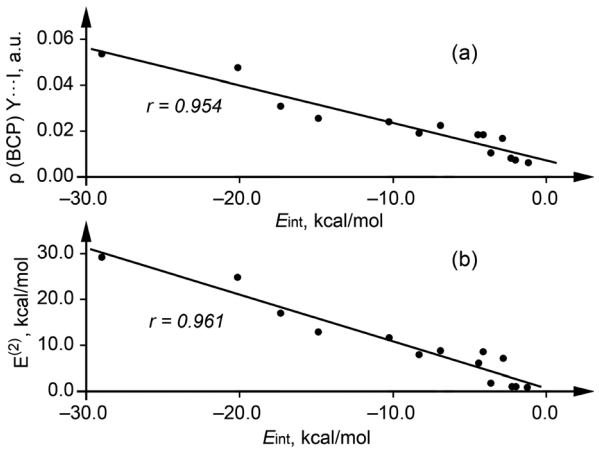

Fig. 6 Regression plots analyzing the correlations in complexes **1–14**. (a) Correlation between the electron density (ρ) at the BCP (in a.u.) and the interaction energy (E_{int}, in kcal mol^{-1}) at the PBE0-D4/def2-TZVP level of theory. (b) Correlation between the LP(Y) → σ*(I–I) ($E^{(2)}$, in kcal mol^{-1}) and the interaction energy (E_{int}, in kcal mol^{-1}) at the PBE0-D4/def2-TZVP level of theory. The correlation coefficients (r) are provided in each plot.

and slope suggest that the variations in binding energy, and specifically the enhancement observed in the trimeric systems, are fundamentally driven by the orbital component of the interaction.

In our analysis of orbital synergy, the NBO $E^{(2)}$ energies are employed to quantify the donor–acceptor interactions between the donor LPs and the σ* antibonding orbitals. It is important to note that while $E^{(2)}$ values provide a reliable descriptor for comparing the relative strength of charge transfer within the **1–14** series, they should be interpreted as semi-quantitative indicators of orbital overlap rather than a direct partition of the total interaction energy.

Crystal structures

The selection of UNOMIV and ZAQZOK as representative solid-state systems was based on a systematic survey of the CSD.[2] These structures were chosen because they exhibit the 2I···I···Nu motif with a minimum number of secondary interactions, facilitating a more direct comparison with the intrinsic electronic properties identified in our optimized model systems. These examples provide essential experimental support to the theoretical investigation while minimizing the energetic noise typically associated with extended supramolecular networks.

While our model systems (**1–14**) focus on small, linear units to isolate the electronic origins of cooperativity, the persistence of the 2I···I···Nu motif in the CSD indicates that this synergy remains viable in more complex molecular environments. As steric bulk increases, the primary challenge for crystal engineering is ensuring that the flanking iodine atoms can reach the equatorial belt of the central donor. Our analysis for UNOMIV and ZAQZOK supports that even with bulky substituents like fluorinated phenyl rings or triiodoimidazole units, the electronic benefits of σ-hole amplification and orbital stabilization are sufficient to stabilize the trifurcated node.

Cooperative effects in a homoleptic system (UNOMIV)

We first analyzed the homoleptic system UNOMIV, which consists of a trimeric assembly of 2,4,5-triiodoimidazole.

MEP analysis of the UNOMIV trimer reveals a clear polarization effect analogous to the $(I_2)_3$ model. The maximum potential at the σ-hole of the central iodine atom increases from 21.9 kcal mol^{-1} in the isolated 2,4,5-triiodoimidazole monomer to 24.8 kcal mol^{-1} in the trimeric assembly (Fig. 7b). This deepening of the σ-hole potential confirms that the donation of electron density from the equatorial belts of the two flanking iodine atoms to the central iodine enhances its electrophilicity, validating the chemical chameleon behavior in this supramolecular architecture.

To confirm the nature of these contacts, we employed NBO analysis combined with QTAIM. The NBO analysis explicitly identifies a charge donation from the LP of the central iodine atom to the antibonding σ*(C–I) orbitals of the two flanking molecules (Fig. 7c). Note that unlike the σ*(I–I) acceptor orbitals in the I_2 models, the acceptor here is the σ*(C–I) orbital, yet the mechanism remains the same. Furthermore, 2D-ELF/QTAIM plots show BCPs and bond paths interconnecting all three iodine atoms, unambiguously confirming the halogen-bonding nature of these interactions (Fig. 7d).

We quantified the cooperative enhancement by comparing the interaction energies of a simple dimer with a larger tetrameric assembly using EDA. The tetramer was constructed to represent the full cooperative node: it includes the 2I···I trimer acting as the donor and a fourth imidazole unit acting as the nucleophile (Fig. 8b). In the isolated dimer (Fig. 8a), the I···I interaction energy is −2.32 kcal mol^{-1}, driven by dispersion and electrostatics due to the high polarizability of iodine.

In the tetrameric assembly, the total interaction energy rises dramatically to −14.88 kcal mol^{-1}. It is important to note that this value includes a contribution from a hydrogen bond formed between the NH group of the acceptor imidazole and a nitrogen atom of the flanking units. By computing the independent energy of this hydrogen-bonded contact (−10.40 kcal mol^{-1}, Fig. 8c) and subtracting it from the total, we isolated the energy of the halogen bond in the cooperative assembly, which is −4.48 kcal mol^{-1}.

Comparing this value (−4.48 kcal mol^{-1}) to the isolated dimer energy (−2.32 kcal mol^{-1}) reveals a net cooperative reinforcement of −2.16 kcal mol^{-1}. This result is striking since the formation of the 2I···I···Nu node nearly doubles the strength of the primary halogen bond compared to the isolated interaction. The component evolution in UNOMIV demonstrates that this doubling is driven by a simultaneous enhancement of electrostatic (E_{el}) and orbital (E_{orb}) terms. Specifically, comparing the isolated dimer (E_{el} = −1.94, E_{orb} = −1.94) to the residual components of the node confirms that the electronic redistribution makes the central iodine atom a superior σ-hole donor and orbital acceptor. This is consistent with NBO results showing charge transfer from the central iodine lone pair to the σ*(C–I) orbitals of the flanking molecules.

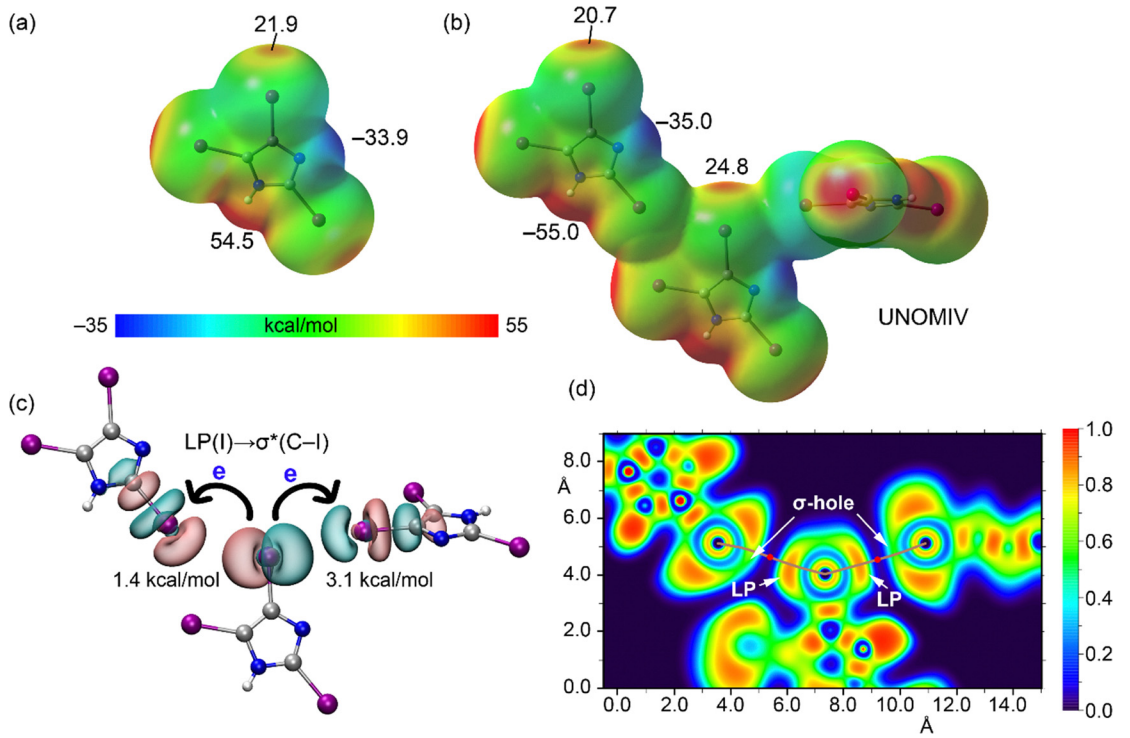

Fig. 7 (a) MEP surface of the 2,4,5-triiodoimidazole monomer. (b) MEP surface of the 2,4,5-triiodoimidazole trimer. (c) NBO analysis showing the charge transfer from the LP of the central iodine atom to the antibonding σ*(C–I) orbitals of the flanking molecules. The energies of these charge transfers are shown in kcal mol^{-1}. (d) 2D-ELF/QTAIM plot of the trimer. The image shows BCPs and bond paths connecting the three iodine atoms.

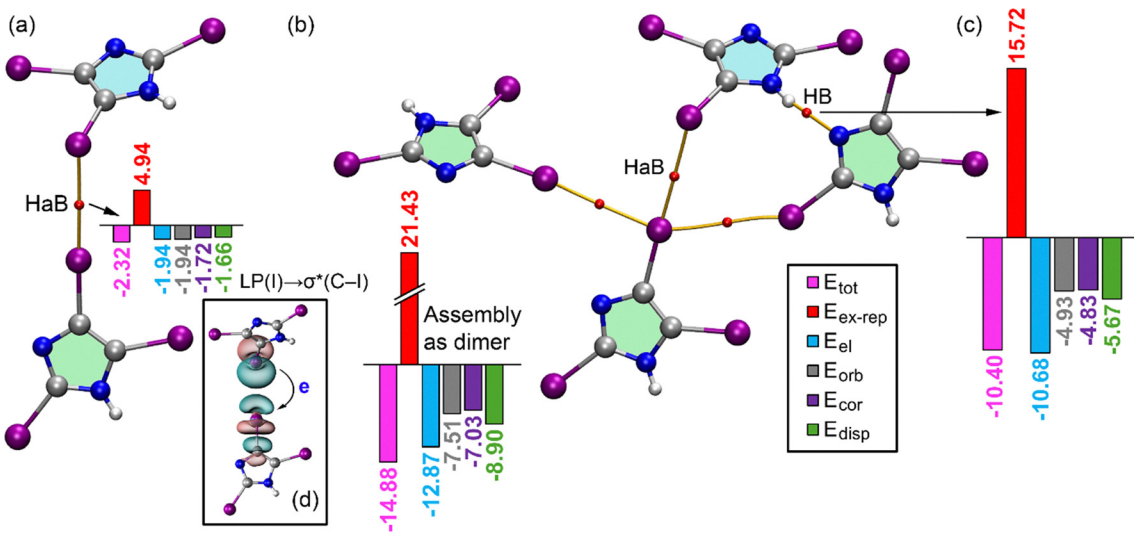

Fig. 8 (a) QTAIM (BCP in red, bond path as orange lines) of the homodimer of 2,4,5-triiodoimidazole with a halogen bond along with the EDA. (b) QTAIM and EDA analysis of the tetrameric assembly of UNOMIV. (c) The EDA for the hydrogen bonded dimer. (d) The inset shows the NBO analysis for the dimer, confirming the charge transfer from the LP of one iodine atom to the σ* antibonding orbital of the other.

Cooperative effects in hetero-atomic nodes

We extended our analysis to the heteroleptic ZAQZOK structure, a cocrystal of 1,3,5-trifluoro-2,4,6-triiodobenzene with 1,3-dithiane. This structure represents the target 2I···I···Nu motif, where Nu is a sulfur atom.

The MEP surfaces of the σ-hole donor molecule and its homotrimer are shown in Fig. 9. The MEP value at the σ-hole increases from 30.1 kcal mol^{-1} in the monomer to 33.9 kcal mol^{-1} in the trimer, providing evidence that the 2I···I motif enhances the electrophilicity of the central iodine atom. NBO analysis (Fig. 9c)

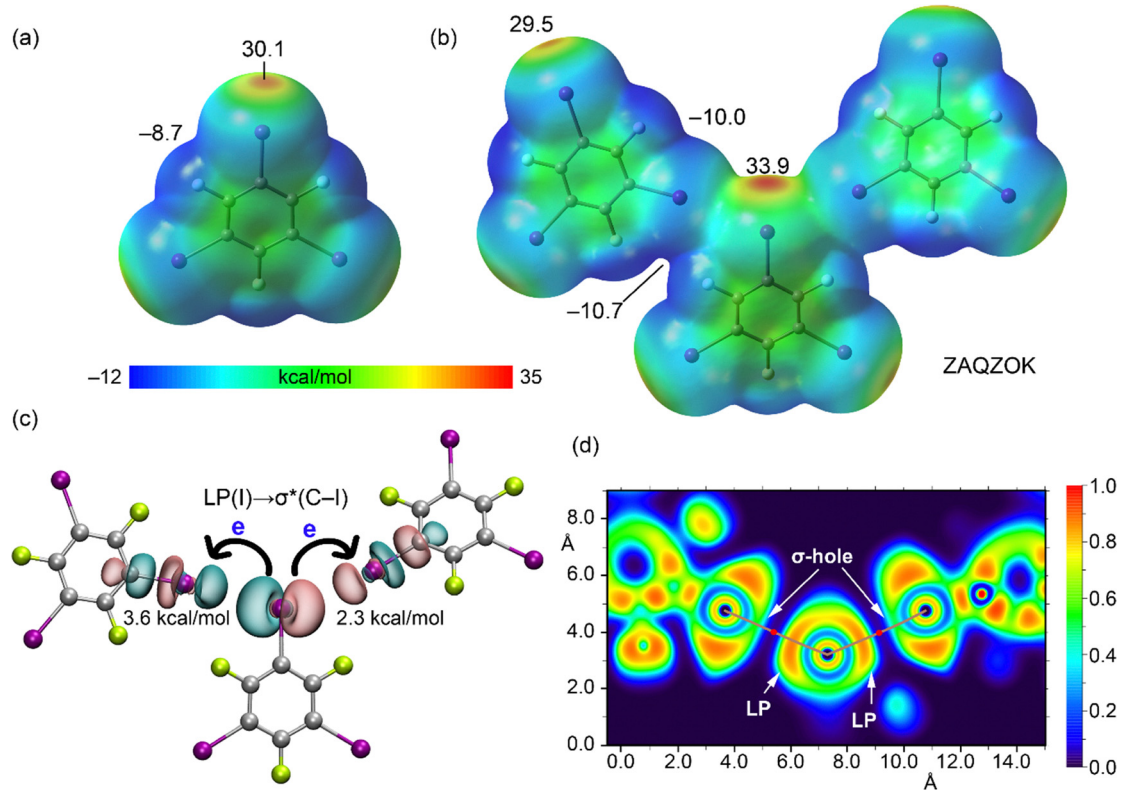

Fig. 9 (a) MEP surface of the 1,3,5-trifluoro-2,4,6-triiodobenzene monomer. (b) MEP surface of the 1,3,5-trifluoro-2,4,6-triiodobenzene trimer. (c) NBO analysis showing the charge transfer from the LP of the central iodine atom to the antibonding σ*(C–I) orbitals of the flanking molecules. The energies of these charge transfers are shown in kcal mol^{-1}. (d) 2D-ELF/QTAIM plot of the trimer. The image shows BCPs and bond paths connecting the three iodine atoms.

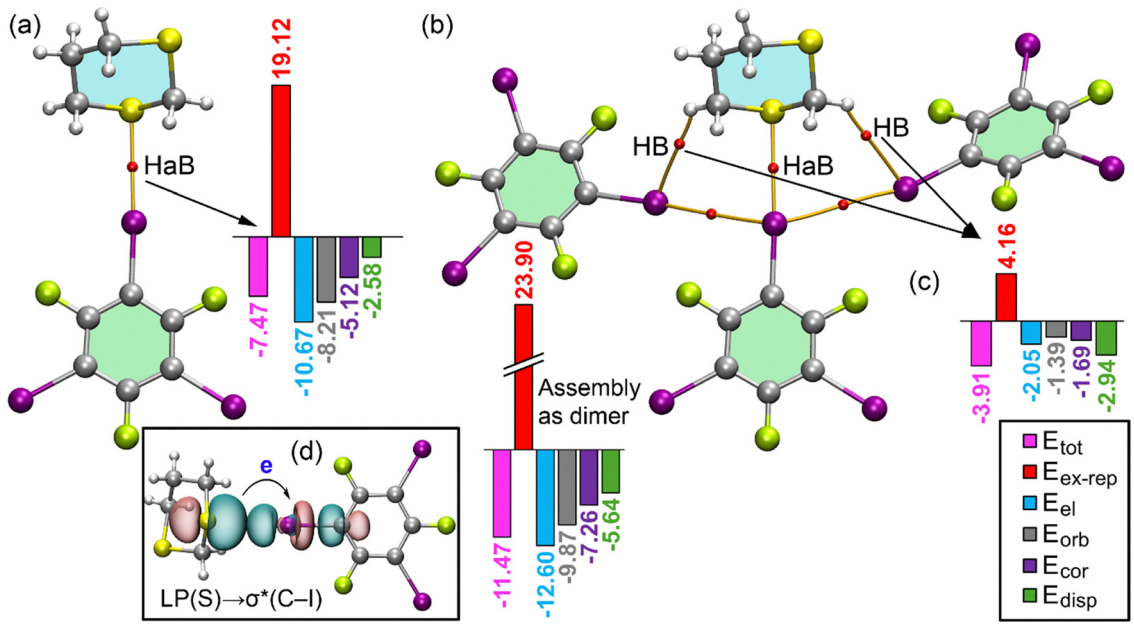

Fig. 10 (a) QTAIM (BCPs in red, bond paths as orange lines) and EDA analyses of the heterodimer dimer of 1,3,5-trifluoro-2,4,6-triiodobenzene with 1,3-dithiane, characterizing the halogen bond in ZAQZOK. (b) QTAIM and EDA analysis of the tetrameric assembly. (c) The combined EDA for both hydrogen bonded dimers. (d) The inset shows the NBO analysis for the dimer, confirming the charge transfer from the LP of one sulfur atom 1,3-dithiane to the σ*(C–I) antibonding orbital of 1,3,5-trifluoro-2,4,6-triiodobenzene.

and 2D-ELF/QTAIM plots confirmed the LP(I) → σ*(C–I) charge transfer from the central iodine atom to the flanking molecules. The ELF also demonstrates that the LP on the central iodine atom points toward the σ-holes of the adjacent iodine atoms. The QTAIM analysis further characterizes the I···I halogen bonds by identifying the corresponding BCPs and bond paths that interconnect the iodine atoms, crossing the LP and entering the σ-holes, which confirms the halogen bonding nature of these contacts.

The energetic analysis for the dimer and tetrameric assemblies of ZAQZOK is presented in Fig. 10. The interaction energy of the heterodimer is –7.47 kcal mol^{-1}, which is significantly larger than the homodimer of UNOMIV because of the superior σ-hole donor and acceptor molecules in ZAQZOK. The energy of the tetrameric assembly, which was calculated as a dimer with the 1,3,5-trifluoro-2,4,6-triiodobenzene trimer acting as one monomer (highlighted in green in Fig. 10b) and 1,3-dithiane as the other, is –11.47 kcal mol^{-1}. In this case, the most dominant attractive term is electrostatic, followed by orbital interactions.

QTAIM analysis also shows that two secondary CH···I contacts contribute to the overall assembly's formation. The contribution of these assemblies has been estimated at –3.91 kcal mol^{-1}, based on the corresponding hydrogen-bonded dimers. Consequently, the reinforcement of the halogen bond within the assembly is only –0.1 kcal mol^{-1}, within the accuracy of the method. This small value indicates negligible cooperativity, especially when compared to the UNOMIV example. This may be due to the interplay between the hydrogen bonds and halogen bonds involving the same iodine atoms of the 2I···I system. In contrast, the hydrogen bond in the UNOMIV example was formed between groups that were not part of the 2I···I motif.

This study demonstrates that subtle changes in the assembly and the presence of secondary interactions can affect the synergy of the 2I···I···Nu interactions, highlighting the need to analyze each case with theoretical tools. Finally, the NBO analysis of the dimer, shown in Fig. 9c, confirms the electron donor role of the 1,3-dithiane and the σ-hole donor role of the 1,3,5-trifluoro-2,4,6-triiodobenzene.

While the subtractive energy scheme provides a useful estimate of cooperative reinforcement, it is important to note its limitations. This approach assumes that individual interactions are additive and may not fully account for complex coupling terms or the influence of secondary contacts. In crystalline systems like ZAQZOK, the presence of competing CH···I interactions likely affects the net synergy. Nevertheless, the consistent trends observed in MEP and NBO analyses across both model and experimental structures confirm that the 2I···I···Nu motif provides a robust electronic foundation for positive cooperativity.

Conclusions

This investigation establishes the energetic foundation for 2I···I···Nu assemblies. Unlike donor-only systems that suffer from negative cooperativity, this mixed donor–acceptor motif operates *via* a mechanism leading to positive cooperativity. The central iodine acts as a chemical chameleon, simultaneously donating density from its equatorial belt while accepting density at its σ-hole.

The key finding of this work is that the central iodine atom in 2I···I···Nu assemblies functions as a genuine chemical chameleon, simultaneously donating electron density through its equatorial belt to two flanking iodine atoms while accepting electron density at its σ-hole from a nucleophile. Our DFT analysis on optimized model systems confirms that this dual behavior is intrinsic to the bonding motif and not merely a product of crystal packing. The formation of a simple $(I_2)_3$ trimer enhances the σ-hole potential of the central iodine by approximately 25% (from 32.6 to 40.8 kcal mol^{-1}) relative to the isolated monomer. This electronic reorganization translates into a consistent strengthening of the interaction with Lewis bases, as evidenced by the computed interaction energies for linear nucleophiles (HF, CO, HCN, OCN^-, SCN^-, and $SeCN^-$), all of which are significantly larger for the trimeric donor than for the monomeric I_2. This trend has been validated by high-level CCSD(T) calculations, which confirm that the observed synergy is a genuine electronic effect and not an artifact of the DFT functional.

NBO analysis reveals that the charge transfer from the central iodine's lone pairs to the antibonding σ* orbitals of the flanking molecules polarizes the central iodine's electron distribution, thereby amplifying its σ–hole depth. Regression analysis of the model systems further establishes that the resulting increase in electron density at the bond critical point is a reliable quantitative predictor of this cooperative strengthening.

We analyzed these intrinsic effects in the solid state by studying the homoleptic UNOMIV and heteroleptic ZAQZOK crystals. In UNOMIV, the cooperative reinforcement amounts to –2.16 kcal mol^{-1} beyond simple additivity, nearly doubling the strength of the isolated I···I interaction. The ZAQZOK system demonstrates that even when secondary contacts like CH···I partially compete with the primary halogen bonds, the 2I···I···Nu motif remains energetically favorable.

In summary, the 2I···I···Nu motif emerges from this study as a structurally and energetically well-defined building block. The positive cooperativity verified here, overcoming the limitations of donor-only systems, establishes these assemblies as robust supramolecular synthons for the rational design of functional materials where directional, tunable noncovalent interactions are required.

Author contributions

Conceptualization: N. B., V. Yu. K., and A. F.; funding acquisition: A. F., investigation: R. G. M., supervision: N. B., V. Yu. K., and A. F.; validation: N. B., V. Yu. K., and A. F.; visualization: R. G. M.; writing – original draft: N. B., V. Yu. K., and A. F.; writing – review and editing: N. B., V. Yu. K., and A. F.

Conflicts of interest

There are no conflicts to declare.

Data availability

The supporting data have been provided as part of the supplementary information (SI). Supplementary information: cartesian coordinates of complexes **1–14**. See DOI: https://doi.org/10.1039/d5cp04988a.

Acknowledgements

NAB and VYK thank the Russian Science Foundation (project 25-13-00035) for support of their studies discussed in this article. A. F. and R. M. G. are grateful to Project PID2023-148453NB-I00 funded by the Ministerio de Ciencia, Innovación y Universidades of Spain MCIU/AEI/10.13039/501100011033 and FEDER, UE.

Notes and references

1 C. S. Z. Vatsadze, Y. D. Loginova, G. dos Passos Gomes and I. V. Alabugin, *Chem. – Eur. J.*, 2017, **23**, 3225–3245.
2 R. M. Gomila, A. Frontera, N. A. Bokach and V. Y. Kukushkin, *Coord. Chem. Rev.*, 2026, **552**, 217465.
3 G. Cavallo, P. Metrangolo, R. Milani, T. Pilati, A. Priimagi, G. Resnati and G. Terraneo, *Chem. Rev.*, 2016, **116**, 2478–2601.
4 G. R. Desiraju, P. S. Ho, L. Kloo, A. C. Legon, R. Marquardt, P. Metrangolo, P. Politzer, G. Resnati and K. Rissanen, *Pure Appl. Chem.*, 2013, **85**, 1711–1713.
5 P. R. Varadwaj, A. Varadwaj, H. M. Marques and K. Yamashita, *Cryst. Growth Des.*, 2024, **24**, 5494–5525.
6 A. Liu and Y.-W. Yang, *Coord. Chem. Rev.*, 2025, **530**, 216488.
7 M. Michalczyk and W. Zierkiewicz, *Phys. Chem. Chem. Phys.*, 2025, **27**, 12248–12255.
8 M. Michalczyk, W. Zierkiewicz and S. Scheiner, *Cryst. Growth Des.*, 2022, **22**, 6521–6530.
9 B. K. Saha, R. V. P. Veluthaparambath and V. G. Krishna, *Chem. – Asian J.*, 2023, **18**, e202300067.
10 J. Marciniak, M. Kaźmierczak, K. W. Rajewski and A. Katrusiak, *Cryst. Growth Des.*, 2016, **16**, 3917–3923.
11 A. J. Peloquin, J. M. McCollum, C. D. McMillen and W. T. Pennington, *Angew. Chem., Int. Ed.*, 2021, **60**, 22983–22989.
12 *TURBOMOLE*, 2024, TURBOMOLE GmbH, Karlsruhe, Germany.
13 C. Adamo and V. Barone, *J. Chem. Phys.*, 1999, **110**, 6158–6170.
14 F. Weigend and R. Ahlrichs, *Phys. Chem. Chem. Phys.*, 2005, **7**, 3297–3305.
15 E. Caldeweyher, S. Ehlert, A. Hansen, H. Neugebauer, S. Spicher, C. Bannwarth and S. Grimme, *J. Chem. Phys.*, 2019, **150**, 154122.
16 K. Kitaura and K. Morokuma, *Int. J. Quantum Chem.*, 1976, **10**, 325–340.
17 E. D. Glendening, C. R. Landis and F. Weinhold, *J. Comput. Chem.*, 2019, **40**, 2234–2241.
18 R. F. W. Bader, *Atoms in Molecules: A Quantum Theory*, Oxford University Press, Oxford, 1990.
19 A. D. Becke and K. E. Edgecombe, *J. Chem. Phys.*, 1990, **92**, 5397–5403.
20 T. Lu and F. Chen, *J. Comput. Chem.*, 2012, **33**, 580–592.
21 F. Neese, *Wiley Interdiscip. Rev.: Comput. Mol. Sci.*, 2025, **15**, e70019.
22 B. Mallada, A. Gallardo, M. Lamanec, B. de la Torre, V. Špirko, P. Hobza and P. Jelinek, *Science*, 2021, **374**, 863–867.